

Atomistic description for temperature-driven phase transitions in BaTiO₃Y. Qi,¹ S. Liu,^{1,2} I. Grinberg,¹ and A. M. Rappe¹¹*Department of Chemistry, The Makineni Theoretical Laboratories, University of Pennsylvania, Philadelphia, Pennsylvania 19104-6323, USA*²*Geophysical Laboratory Carnegie Institution for Science, Washington, DC 20015, USA*

(Received 8 January 2016; revised manuscript received 26 August 2016; published 19 October 2016)

Barium titanate (BaTiO₃) is a prototypical ferroelectric perovskite that undergoes the rhombohedral-orthorhombic-tetragonal-cubic phase transitions as the temperature increases. In this paper, we develop a classical interatomic potential for BaTiO₃ within the framework of the bond-valence theory. The force field is parametrized from first-principles results, enabling accurate large-scale molecular dynamics (MD) simulations at finite temperatures. Our model potential for BaTiO₃ reproduces the temperature-driven phase transitions in isobaric-isothermal ensemble (*NPT*) MD simulations. This potential allows for the analysis of BaTiO₃ structures with atomic resolution. By analyzing the local displacements of Ti atoms, we demonstrate that the phase transitions of BaTiO₃ exhibit a mix of order-disorder and displacive characters. Besides, from a detailed observation of structural dynamics during phase transition, we discover that the global phase transition is associated with changes in the equilibrium value and fluctuations of each polarization component, including the ones already averaging to zero. Contrary to the conventional understanding that temperature increase generally causes bond-softening transition, the *x*-polarization component (the one which is polar in both the orthorhombic and the tetragonal phases) exhibits a bond-hardening character during the orthorhombic-to-tetragonal transition. These results provide further insight about the temperature-driven phase transitions in BaTiO₃.

DOI: [10.1103/PhysRevB.94.134308](https://doi.org/10.1103/PhysRevB.94.134308)**I. INTRODUCTION**

Barium titanate (BaTiO₃) is a ferroelectric perovskite with promising applications in electronic devices, such as non-volatile memory, high- κ dielectrics, and piezoelectric sensors [1–4]. Therefore, it is of great significance to investigate and understand the structural and electronic properties of BaTiO₃ for designed material optimization and device engineering. First-principles density functional theory (DFT) has served as a powerful method for understanding the electronic structures of ferroelectric materials [5–10]. Due to the expensive computational cost, the application of DFT methods is currently limited to systems of fairly small size at zero kelvin. Many important dynamical properties, such as domain-wall motions and temperature-driven phase transitions, are beyond the capability of conventional first-principles methods. An effective Hamiltonian method was developed to study the finite-temperature properties of BaTiO₃ [11–14]. To apply this method, the subset of dynamical modes that determine a specific property should be known *a priori*. Molecular dynamics (MD) simulations with an atomistic potential accounting for all the modes offer distinct advantages, especially in providing detailed information about atomic positions, velocities, and modifications of chemical bonds due to a chemical reaction or thermal excitation. The shell model for BaTiO₃ has been developed [15–19]. However, due to the low mass assigned to the shell, a small time step in MD simulations is required to achieve accurate results, which limits the time and length scales of the simulations.

Recently, we developed a bond-valence (BV) model potential for oxides based on the bond-valence theory [20–24]. The force fields for many technologically important ferroelectric materials, PbTiO₃, PbZrO₃, and BiFeO₃ [20,22–26], have been parametrized based on the results from DFT calculations. A typical force field requires no more than 15 parameters and can be efficiently implemented, which enables simulations of

systems with thousands of atoms under periodic boundary conditions [27,28]. The development of an accurate classical potential for BaTiO₃ has proven to be difficult, mainly due to the small energy differences among the four phases (rhombohedral, orthorhombic, tetragonal, and cubic) [29–31]. In this paper, we apply the bond-valence model to BaTiO₃ and parametrize the all-atom interatomic potential to first-principles data. Our model potential for BaTiO₃ is able to reproduce the rhombohedral-orthorhombic-tetragonal-cubic phase-transition sequence in isobaric-isothermal ensemble (*NPT*) MD simulations. The phase-transition temperatures agree reasonably well with previous theoretical results [15]. We further examine the temperature dependence of the local displacements of Ti atoms and discover several features of the phase transitions of BaTiO₃: The phase transitions of BaTiO₃ involve both order-disorder and displacive characters; at the moment that the phase transition of the crystal occurs, all the polarization components undergo phase transitions, even for the nonpolar ones, and temperature increase can also cause bond hardening for a certain component.

II. METHODS

The bond-valence model potential is developed based on the conservation principles of the bond valence and the bond-valence vector (BVV). The bond-valence V_{ij} reflects the bonding strength and can be calculated based on the bond length r_{ij} with [20–24,32–34]

$$V_{ij} = \left(\frac{r_{0,ij}}{r_{ij}} \right)^{C_{ij}}, \quad (1)$$

where i and j are the labels for atoms; $r_{0,ij}$ and C_{ij} are Brown's empirical parameters. The bond-valence vector is defined as a vector lying along the bond $\mathbf{V}_{ij} = V_{ij} \hat{\mathbf{R}}_{ij}$, where $\hat{\mathbf{R}}_{ij}$ is the unit vector pointing from atom i to atom j . The total energy

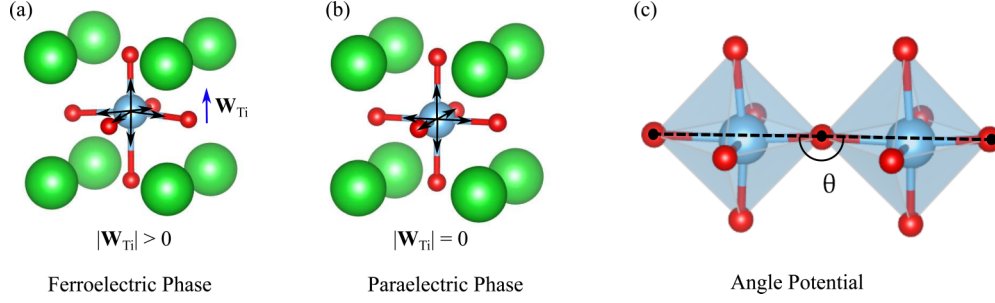


FIG. 1. Bond-valence vector sum and angle potential. (a) Tetragonal BaTiO₃ with a nonzero BVVS; (b) cubic BaTiO₃ with zero BVVS; (c) schematic of the angle potential. Ba, Ti, and O atoms are represented by green, blue, and red spheres, respectively.

(E) consists of the Coulombic energy (E_c), the short-range repulsive energy (E_r), the bond-valence energy (E_{BV}), the bond-valence vector energy (E_{BVV}), and the angle potential (E_a) [21–24],

$$E = E_c + E_r + E_{\text{BV}} + E_{\text{BVV}} + E_a, \quad (2)$$

$$E_c = \sum_{i < j} \frac{q_i q_j}{r_{ij}}, \quad (3)$$

$$E_r = \sum_{i < j} \left(\frac{B_{ij}}{r_{ij}} \right)^{12}, \quad (4)$$

$$E_{\text{BV}} = \sum_i S_i (V_i - V_{0,i})^2, \quad (5)$$

$$E_{\text{BVV}} = \sum_i D_i (\mathbf{W}_i^2 - \mathbf{W}_{0,i}^2)^2, \quad (6)$$

$$E_a = k \sum_i^{N_{\text{oxygen}}} (\theta_i - 180^\circ)^2, \quad (7)$$

where $V_i = \sum_{j \neq i} V_{ij}$ is the bond-valence sum (BVS), $\mathbf{W}_i = \sum_{j \neq i} \mathbf{V}_{ij}$ is the bond-valence vector sum [(BVVS), shown in Figs. 1(a) and 1(b)], q_i is the ionic charge, B_{ij} is the short-range repulsion parameter, S_i and D_i are scaling parameters with the unit of energy, k is the spring constant, and θ is the O-O-O angle along the common axis of two adjacent oxygen octahedra [Fig. 1(c)]. The bond-valence energy E_{BV} captures the energy penalty for both overbonded and underbonded atoms. The bond-valence vector energy E_{BVV} is a measure of the breaking of local symmetry, which is important for correctly describing the ferroelectricity. $V_{0,i}$ and $\mathbf{W}_{0,i}$ are preferred or target values of BVS and BVVS for atom i in the ground-state structure, which can be calculated from DFT directly. It is noted that the E_{BV} and E_{BVV} can be related to the moments of the local density of states in the framework of a tight-binding model,

providing a quantum-mechanical justification for these two energy terms [23,24,32,35,36]. The angle potential is used to account for the energy cost associated with the rotations of oxygen octahedra.

We followed the optimization protocol developed in previous studies [23,24]. The optimal values of force-field parameters q_i , S_i , D_i , and B_{ij} are acquired by minimizing the difference between the DFT energies/forces and the model-potential energies/forces for a database of BaTiO₃ structures. All DFT calculations are carried out with the plane-wave DFT package QUANTUM-ESPRESSO [37] using the Perdew-Burke-Ernzerhof functional modified for solids (PBEsol) [38] and optimized norm-conserving pseudopotentials generated by the OPIUM package [39]. A plane-wave cutoff energy of 50 Ry and a $4 \times 4 \times 4$ Monkhorst-Pack k -point mesh [40] are used for energy and force calculations. The database consists of 40-atom $2 \times 2 \times 2$ supercells with different lattice constants and local ion displacements. The final average difference between DFT energy and model-potential energy is 1.35 meV/atom.

III. PERFORMANCE OF THE CLASSICAL POTENTIAL

The optimized parameters are listed in Table I. The performance of the obtained force field is examined by investigating the temperature dependence of lattice constants (a , b , and c), component-resolved local displacements of Ti atoms (d_x , d_y , and d_z), and the three components of the total polarization (P_x , P_y , and P_z). We carried out NPT MD simulations using a $10 \times 10 \times 10$ supercell (5000 atoms) with the temperature controlled via the Nosé-Hoover thermostat and the pressure maintained at 1 atm via the Parrinello-Rahman barostat [41]. Each simulation was performed for 80 ps with a 1-fs time step. The thermal inertia parameter M_s was selected as 1.0 amu for the first 20 ps and 5.0 amu for the remaining 60 ps. The local polarization of each unit-cell $\mathbf{P}_u(t)$ is

TABLE I. Optimized force field for BaTiO₃. The angle constant $k = 6.1$ meV/(deg)².

	$r_{0,\beta\text{O}}$	$C_{0,\beta\text{O}}$	q_β (e)	S_β (eV)	D_β	$B_{\beta\beta'}$ (Å)			$V_{0,\beta}$	$\mathbf{W}_{0,\beta}$
						Ba	Ti	O		
Ba	2.290	8.94	1.34730	0.59739	0.08429	2.44805	2.32592	1.98792	2.0	0.11561
Ti	1.798	5.20	1.28905	0.16533	0.82484		2.73825	1.37741	4.0	0.39437
O			-0.87878	0.93063	0.28006			1.99269	2.0	0.31651

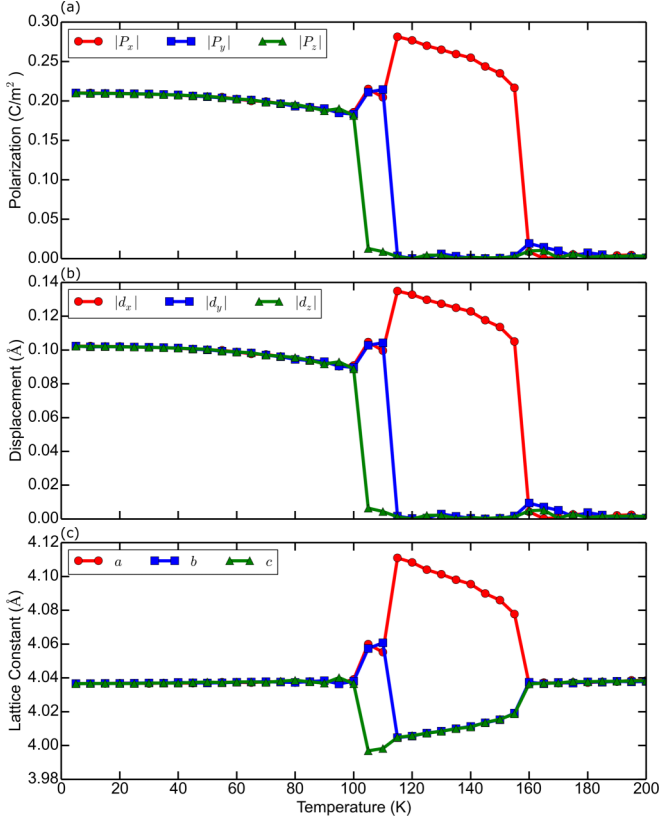


FIG. 2. Temperature dependence of the polarization, Ti displacement, and lattice constants in BaTiO₃. Phase transitions among rhombohedral, orthorhombic, tetragonal, and cubic occur at 105, 115, and 160 K.

expressed as

$$\mathbf{P}_u(t) = \frac{1}{V_u} \left(\frac{1}{8} \mathbf{Z}_{\text{Ba}}^* \sum_{i=1}^8 \mathbf{r}_{\text{Ba},i}(t) + \mathbf{Z}_{\text{Ti}}^* \mathbf{r}_{\text{Ti}}(t) + \frac{1}{2} \mathbf{Z}_{\text{O}}^* \sum_{i=1}^6 \mathbf{r}_{\text{O},i}(t) \right), \quad (8)$$

where V_u is the volume of a unit cell, \mathbf{Z}_{Ba}^* , \mathbf{Z}_{Ti}^* , and \mathbf{Z}_{O}^* are the Born effective charges of the Ba, Ti, and O atoms with $\mathbf{Z}_{\text{Ba}}^* = 2.9$, $\mathbf{Z}_{\text{Ti}}^* = 6.7$, and $\mathbf{Z}_{\text{O}}^* = \frac{1}{3}(\mathbf{Z}_{\text{Ba}}^* + \mathbf{Z}_{\text{Ti}}^*)$ [42]. $\mathbf{r}_{\text{Ba},i}(t)$, $\mathbf{r}_{\text{Ti}}(t)$, and $\mathbf{r}_{\text{O},i}(t)$ are the positions of the Ba, Ti, and O atoms at time t .

As shown in Fig. 2, the simulations clearly reveal four distinct phases under different temperature ranges and three first-order phase transitions. Below 100 K, the displacements of Ti atoms and the overall polarization of the supercell are along the [111] direction ($P_x = P_y = P_z$), characteristic of the rhombohedral phase. At 100 K, the z component of the total

TABLE II. Comparison of the phase-transition temperatures given by the BV model, the shell model [15], and experiments [44].

	R-O (K)	O-T (K)	T-C (K)
BV model	100	110	160
Shell model	80	120	170
Experiments	183	278	393

TABLE III. Comparison of lattice constants of BaTiO₃ given by MD simulations with the BV model potential and PBEsol DFT calculations. For MD simulations, lattice constants of rhombohedral, orthorhombic, tetragonal, and cubic phases are obtained at 5, 105, 120, and 165 K, respectively. Since DFT neglects thermal expansion, the results given by MD simulations, which are larger but less than 1%, demonstrate that this set of potentials can predict the lattice constants of BaTiO₃ quite well.

Lattice constant	MD (Å)	DFT (Å)	Error (%)
Rhombohedral			
$a = b = c$	4.036	4.024	0.30
Orthorhombic			
a	3.997	3.977	0.50
$b = c$	4.059	4.046	0.32
Tetragonal			
$a = b$	4.005	3.985	0.50
c	4.109	4.089	0.49
Cubic			
$a = b = c$	4.037	4.002	0.87

polarization P_z becomes approximately 0, indicating a phase transition from rhombohedral to orthorhombic ($P_x = P_y > 0$, $P_z = 0$). As the temperature increases further to 110 K, the total polarization aligns preferentially along the x direction ($P_x > 0$, $P_y = P_z = 0$), and the lattice constants have $b = c < a$. The supercell stays tetragonal until 160 K at which point the ferroelectric-paraelectric phase transition occurs. The phase-transition temperatures match well with those predicted by the shell model [15] (Table II). Experimental phase-transition temperatures are also listed in Table II. It can be seen that phase-transition temperatures are consistently underestimated in our MD simulations. This underestimation has been observed previously in other DFT fitted simulations and is due to the systematic error of exchange-correlation functional used for force-field optimization [12,23,43,44]. The accuracy of DFT depends on exchange-correlation functionals. Using different exchange-correlation functionals in parametrization affects the simulated phase-transition temperatures, but nearly all DFT calculations underestimate the energy barriers between states corresponding to different phases [44]. There are *ad hoc* techniques for fixing this problem, such as scaling the *ab initio* energy surface [44] or using a negative pressure [12]. These techniques would not be discussed detailedly in this paper because the underestimation does not affect the practical application of this potential much [23–25,28]. We extract the averaged lattice constants at finite temperatures from MD simulations and find that they are in good agreement (error less than 1%) with the PBEsol values (Table III).

Domain walls are interfaces separating domains with different polarities. They are important topological defects and can be moved by applying an external stimulus [27,28]. The domain-wall energy for a 180° wall obtained from our MD simulations is 6.63 mJ/m², which is comparable to the PBEsol value of 7.84 mJ/m². This indicates that our atomistic potential can be used for studying the dynamics of ferroelectric domain walls in BaTiO₃. All these results demonstrate the robustness of this developed classical potential. By using this

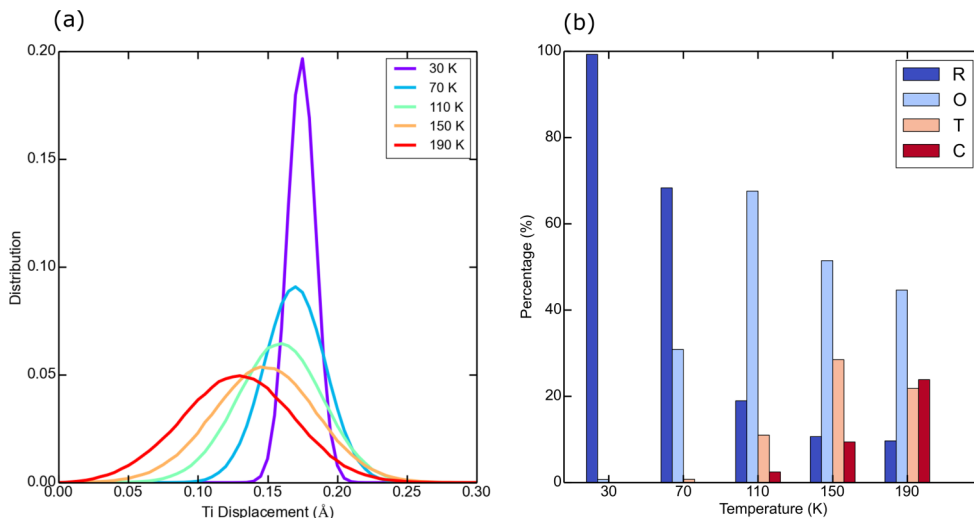


FIG. 3. (a) The distribution of total Ti displacement magnitude at different temperatures. (b) Instantaneous compositions of different phases. Supercells at 30 K (rhombohedral), 70 K (rhombohedral), 110 K (orthorhombic), 150 K (tetragonal), and 190 K (cubic) are studied. Heights of the dark blue, light blue, orange, and red rectangles represent the percentages of rhombohedral, orthorhombic, tetragonal, and cubic unit cells, respectively. The phases of the unit cells are categorized by their Ti displacements d : for $d < 0.1 \text{ \AA}$, the unit cell is considered as a nonpolar one; for a polar unit cell, if one component is larger than $d/\sqrt{6}$, then this component is considered a ferroelectric one. The ferroelectric phase (tetragonal, orthorhombic, and rhombohedral) is determined by the number of ferroelectric components.

potential, we can calculate real experimental observables, such as dielectric constant, frequency-dependent dielectric response, vibrational modes, and their temperatures, pressures, and stress dependences. In the following section, we will discuss atomistic features of BaTiO₃ phase transitions.

IV. ATOMISTIC FEATURES OF DIFFERENT PHASES

To provide an atomistic description of the different phases of BaTiO₃, we analyze the distribution of local displacements of Ti atoms in each phase. Ti displacement is defined as the distance between the Ti atom and the center of the oxygen octahedral cage of a unit cell, which scales with the magnitude of polarization.

In Fig. 3(a), we plot the distributions of Ti displacements ($d = \sqrt{d_x^2 + d_y^2 + d_z^2}$). It can be seen that, in all four phases, the distribution is approximately a Gaussian curve, whose peak shifts toward lower values as the temperature increases. This suggests that the temperature-driven phase transition has a displacive character. It is noted that the distribution of magnitudes is peaked at nonzero values even in the paraelectric cubic phase, suggesting that most Ti atoms are still locally displaced at high temperatures and that the overall net zero polarization is the result of an isotropic distribution

TABLE IV. Relative energies (potential energies) of different phases from DFT calculations. The cubic unit cell is chosen as the reference structure.

	Rhombohedral	Orthorhombic	Tetragonal	Cubic
Energy (meV/unit cell)	-39.31	-37.23	-29.47	0

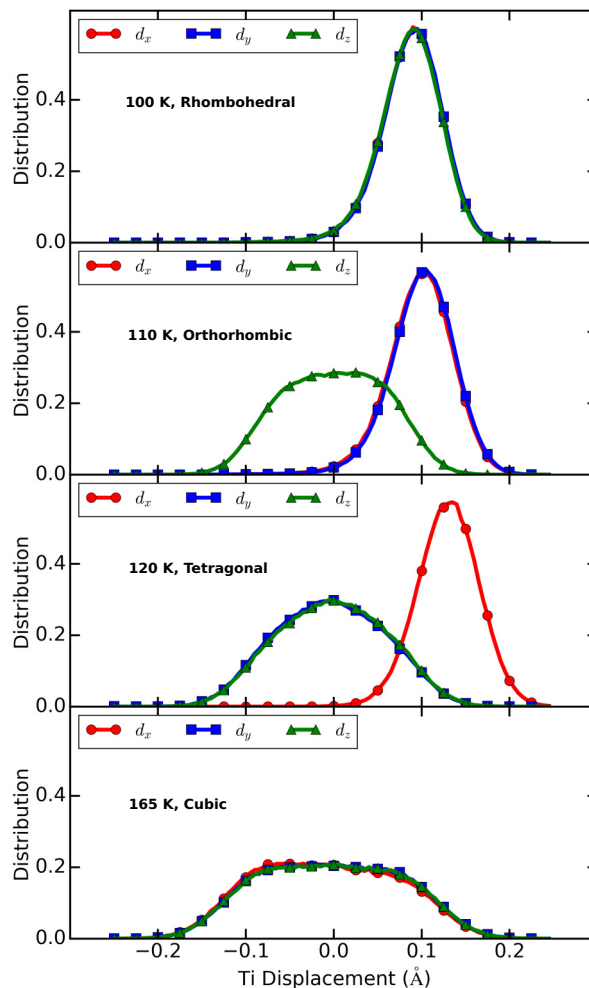


FIG. 4. The distributions of Ti displacement at different temperatures.

of local dipoles along different directions. This confirms the order-disorder character for BaTiO₃ at high temperatures.

We can categorize the instantaneous phase of each unit cell based on the local displacement of a Ti atom. The categorization criteria are as follows:

- (1) If $d < 0.1 \text{ \AA}$, the unit cell is considered to be paraelectric cubic;
- (2) For a ferroelectric unit cell, the k th component is considered to be ferroelectric if $d_k > d/\sqrt{6}$. The rhombohedral, orthorhombic, and tetragonal unit cells have three, two, and one ferroelectric component(s), respectively.

The results are shown in Fig. 3(b). At 30 K, the supercell is made only from rhombohedral unit cells, showing that the rhombohedral phase is the ground-state structure. As the temperature increases, the supercell becomes a mixture of the four phases. It should be noted that the cubic unit cell with nearly zero local Ti displacement seldom appears because a cubic unit cell is energetically less favorable. The relative energies of the four phases of BaTiO₃ from PBEsol DFT calculations are listed in Table IV. It can be seen that the energy differences among the tetragonal, orthorhombic, and rhombohedral unit cells are small (within several meV per unit cell) [5,45]. Due to the thermal fluctuations, the populations of higher-energy ferroelectric phases (tetragonal and orthorhombic) increase as temperature increases. Above

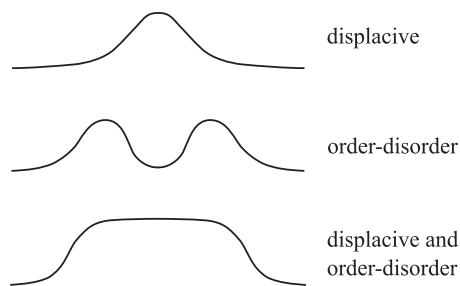


FIG. 5. Schematic of the distributions of Ti displacement for displacive transition, order-disorder transition, and a mix of them.

the ferroelectric-paraelectric transition temperature, locally ferroelectric unit cells are still favored over paraelectric ones due to the relatively high energy of the cubic high-symmetry structure.

In Fig. 4, the distributions of Ti displacements along the three axes are plotted. At 100 K, BaTiO₃ is at the rhombohedral phase, and the distributions of Ti displacements are Gaussian-like. As the temperature increases, the phase changes to orthorhombic. The average of the z -polarization component shifts to zero, indicating a displacive phase transition. Besides, the standard deviation increases, and the center of the distribution curve becomes flatter. For the cubic phase,

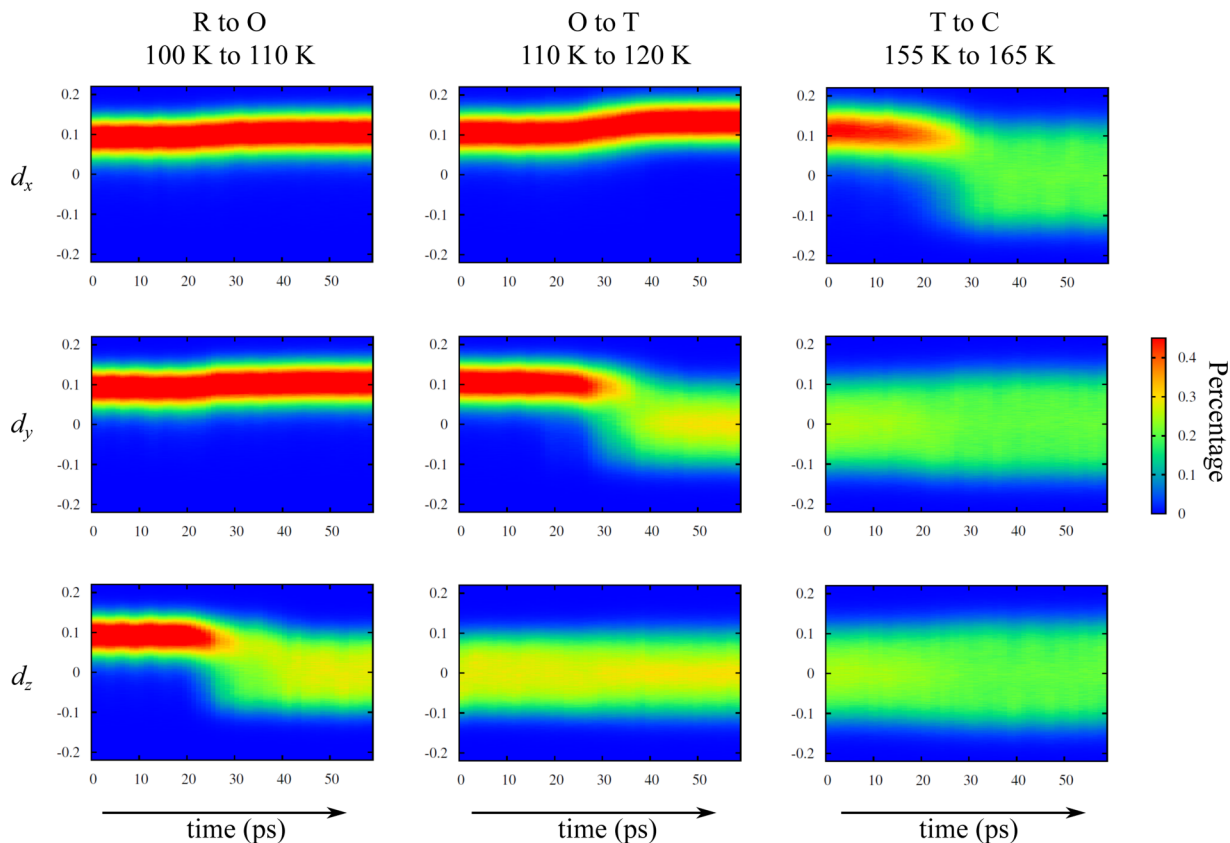


FIG. 6. Temperature dependence of Ti displacement distributions in three Cartesian directions. The horizontal axis shows the time. In these simulations, the temperature increases with time approximately linearly. The vertical axis represents the fraction of the Ti displacements, and the color scale represents the percentages of Ti displacement with a certain value. Note that, in the bottom center plot, the color showing the distribution becomes redder after the orthorhombic-to-tetragonal transition, indicating a narrower distribution around $d_z = 0$ and a bond hardening in this direction.

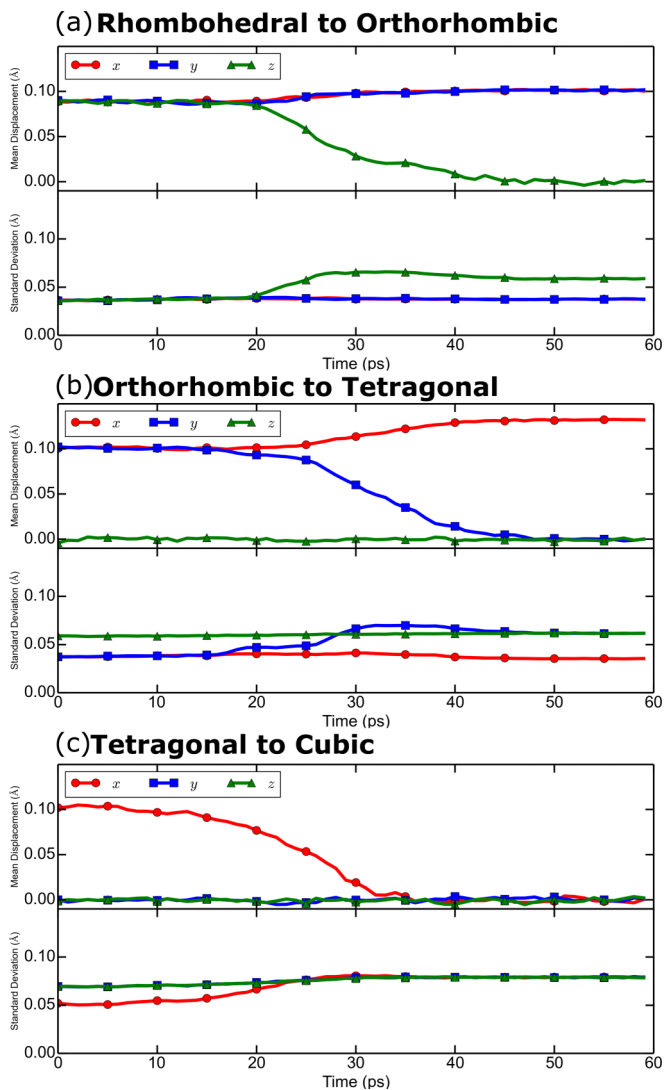


FIG. 7. The change in the average and standard deviations of the Ti displacement distribution. In the standard deviation plot of (b), the green and black lines increase with temperature and are parallel until the transition.

the center of the Ti displacement distribution curve is also flat. As shown in Fig. 5, the center-flat curve is a summation of a Gaussian curve centering at zero and a double-peak curve. The latter is characteristic of order-disorder transition [27]. These results further demonstrate that phase transitions of BaTiO₃ have a mix of order-disorder and displacive characters [29,46–51].

V. FEATURES OF THE PHASE TRANSITIONS

To investigate the structural dynamics during phase transitions in more detail, we conducted MD simulations with varying temperatures. In three different sets of simulations, the temperatures were increased from 100 to 110 K (*R* to *O*), 110 to 120 K (*O* to *T*), and 155 to 165 K (*T* to *C*), respectively. The temperature was controlled by the Nosé-Hoover thermostat with a thermal inertia parameter $M_s = 10$, and the 10-K

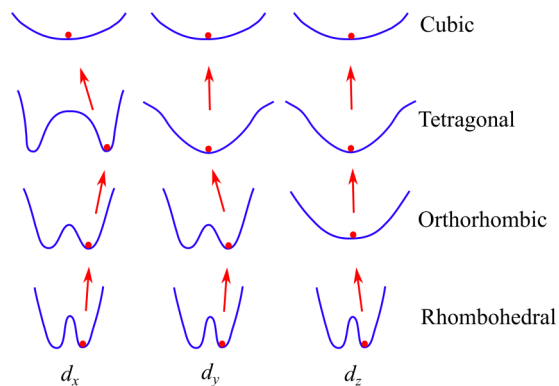


FIG. 8. Schematics of bond-softening, bond-hardening, and displacive excitations. Two points worth mentioning: (1) For the *x* component (first column), the minima of the energy profile for the tetragonal phase are further from the center and have higher curvatures, compared with those for the orthorhombic phase because the Ti displacement distribution has a larger average and smaller variance; (2) for the *z* component (third column), compared with the energy profile for orthorhombic phase, the one for the tetragonal phase has a higher curvature at the center (Ti displacement more closely distributed around 0 as seen from Fig. 6) and smaller curvature for larger *z*-direction displacements [larger standard deviation, seen from Fig. 7(b)].

temperature change was accomplished in 60 ps. We analyze the temperature dependence of Ti displacement distributions along three axes. The dynamics of Ti displacement distributions during the phase transitions are plotted in Fig. 6. The time evolution of the average and standard deviations of the Ti displacement distributions are shown in Fig. 7.

Phase transition occurs when one component undergoes polar-nonpolar transition. The first column (from 100 to 110 K) shows the changes in Ti displacement distributions during the rhombohedral-to-orthorhombic phase transition. In the *x* and *y* directions, the averages of the distribution shift up, which is a characteristic of displacive transition. Meanwhile, in the *z* direction, the average becomes zero, and the variance becomes significantly larger, indicating that the transition is a mix of displacive and bond-softening characters [52]. For the orthorhombic-to-tetragonal phase transition (second column), the transition of the *y* component, which is a polar-nonpolar transition, includes both displacive and bond-softening features. For the *x* component, the transition involves both an increase in the average and a decrease in the standard deviation. For the *z* direction, even though the Ti displacement distribution is centered at zero above and below the transition, the Ti displacements are located closer to zero, indicating an increase in bond hardness. From 155 to 165 K, there is also a bond-hardness-changing transition for the components (*x* and *y*) with zero averages. We collectively refer to bond softening and bond hardening as bond-hardness changing.

Based on the features of the Ti displacement distributions at different phases, the schematic of the thermal excitation between different energy surfaces is presented in Fig. 8. From our results, the characteristics of BaTiO₃ phase transition can be summarized as: (1) For BaTiO₃, the mechanisms of

TABLE V. Phase-transition characters of each component. Hardness changing includes bond softening and bond hardening, which are characterized by the change in the standard deviation of the Ti displacement distribution.

Component	R to O			O to T			T to C		
	d_x	d_y	d_z	d_x	d_y	d_z	d_x	d_y	d_z
Hardness changing	N	N	Y	Y	Y	Y	Y	Y	Y
Displacive	Y	Y	Y	Y	Y	N	Y	N	N

phase transitions include both bond-hardness changing and displacive transition. The sudden shifts of the average and standard deviations correspond to displacive transition with some order-disorder contribution and bond-hardness-changing transitions, respectively; (2) unlike the conventional understanding that thermal excitation usually causes bond softening, increasing temperature can also cause bond hardening. The x component of polarization during the orthorhombic-to-tetragonal transition is an example of this case. (3) When the phase transition occurs, each component of polarization undergoes a change, even for the component(s) which is (are) nonpolar before and after the transition. The transition(s) that each component undergoes are listed in Table V.

In phenomenological models, people use order parameters, such as polarization or any mode, to describe the free energy [53,54]. Geneste pointed out that free energy should be expressed with the density of probability (DOP) of the order parameter rather than local order parameters [43]. DOP is defined as the average of the order parameters in a given region and is characterized by its standard deviation. Our simulation is consistent with this paper, and all these results demonstrate that both the average and the standard deviations of the polarization distribution are features of each specific phase.

VI. CONCLUSION

In this paper, we develop a classical atomistic potential for BaTiO₃ based on the bond-valence model. Molecular dynamics simulation with this optimized potential cannot only reproduce the temperature-driven phase transitions, but also can be a powerful tool in studying the phase-transition process with high temporal and spatial resolutions. The detailed analysis of the local displacements of Ti atoms reveals that, in each phase (including the paraelectric phase), the majority of Ti atoms is locally displaced and the phase transitions in BaTiO₃ exhibit a mixture of order-disorder and displacive character. The distribution of Ti displacement is a Gaussian curve or a curve involving a Gaussian and a double-peak one. By analyzing the dynamics of Ti displacement distributions during phase transition, we discover several rules of BaTiO₃ phase transitions: The global phase transition is associated with significant changes in each component, even for the components which are nonpolar, and the orthorhombic-to-tetragonal transition exhibits a bond-hardening character in the x component, which is opposite from the conventional understanding that temperature increases generally cause bond-softening transition.

ACKNOWLEDGMENTS

Y.Q. was supported by the U.S. National Science Foundation, under Grant No. CMMI1334241. S.L. was supported by the U.S. National Science Foundation, under Grant No. CBET1159736 and the Carnegie Institution for Science. I.G. was supported by the Office of Naval Research, under Grant No. N00014-12-1-1033. A.M.R. was supported by the Department of Energy, under Grant No. DE-FG02-07ER46431. Computational support was provided by the High-Performance Computing Modernization Office of the Department of Defense and the National Energy Research Scientific Computing Center of the Department of Energy.

-
- [1] W. S. Yun, J. J. Urban, Q. Gu, and H. Park, *Nano Lett.* **2**, 447 (2002).
 - [2] K.-H. Chen, Y.-C. Chen, Z.-S. Chen, C.-F. Yang, and T.-C. Chang, *Appl. Phys. A Mater. Sci.* **89**, 533 (2007).
 - [3] W. Buessem, L. Cross, and A. Goswami, *J. Am. Ceram. Soc.* **49**, 33 (1966).
 - [4] T. Karaki, K. Yan, and M. Adachi, *Jpn. J. Appl. Phys.* **46**, 7035 (2007).
 - [5] R. E. Cohen, *Ferroelectrics* **136**, 65 (1992).
 - [6] X. Gonze and C. Lee, *Phys. Rev. B* **55**, 10355 (1997).
 - [7] S. Saha, T. P. Sinha, and A. Mookerjee, *Phys. Rev. B* **62**, 8828 (2000).
 - [8] A. M. Kolpak, D. Li, R. Shao, A. M. Rappe, and D. A. Bonnell, *Phys. Rev. Lett.* **101**, 036102 (2008).
 - [9] J. M. P. Martirez, E. H. Morales, W. A. Saidi, D. A. Bonnell, and A. M. Rappe, *Phys. Rev. Lett.* **109**, 256802 (2012).
 - [10] E. H. Morales, J. M. P. Martirez, W. A. Saidi, A. M. Rappe, and D. A. Bonnell, *ACS Nano* **8**, 4465 (2014).
 - [11] W. Zhong, D. Vanderbilt, and K. M. Rabe, *Phys. Rev. Lett.* **73**, 1861 (1994).
 - [12] W. Zhong, D. Vanderbilt, and K. M. Rabe, *Phys. Rev. B* **52**, 6301 (1995).
 - [13] T. Nishimatsu, U. V. Waghmare, Y. Kawazoe, and D. Vanderbilt, *Phys. Rev. B* **78**, 104104 (2008).
 - [14] H. Fu and L. Bellaiche, *Phys. Rev. Lett.* **91**, 257601 (2003).
 - [15] S. Tinte, M. G. Stachiotti, M. Sepiarsky, R. L. Migoni, and C. O. Rodriguez, *J. Phys.: Condens. Matter* **11**, 9679 (1999).
 - [16] S. Tinte and M. G. Stachiotti, *Phys. Rev. B* **64**, 235403 (2001).
 - [17] S. Tinte, M. Stachiotti, M. Sepiarsky, R. Migoni, and C. Rodriguez, *Ferroelectrics* **237**, 41 (2000).
 - [18] Y. Zhang, J. Hong, B. Liu, and D. Fang, *Nanotechnology* **21**, 015701 (2010).
 - [19] Y. Zhang, J. Hong, B. Liu, and D. Fang, *Nanotechnology* **20**, 405703 (2009).
 - [20] I. Grinberg, V. R. Cooper, and A. M. Rappe, *Nature (London)* **419**, 909 (2002).

- [21] Y.-H. Shin, J.-Y. Son, B.-J. Lee, I. Grinberg, and A. M. Rappe, *J. Phys.: Condens. Matter* **20**, 015224 (2008).
- [22] Y.-H. Shin, V. R. Cooper, I. Grinberg, and A. M. Rappe, *Phys. Rev. B* **71**, 054104 (2005).
- [23] S. Liu, I. Grinberg, and A. M. Rappe, *J. Physics.: Condens. Matter* **25**, 102202 (2013).
- [24] S. Liu, I. Grinberg, H. Takenaka, and A. M. Rappe, *Phys. Rev. B* **88**, 104102 (2013).
- [25] F. Chen, J. Goodfellow, S. Liu, I. Grinberg, M. C. Hoffmann, A. R. Damodaran, Y. Zhu, P. Zalden, X. Zhang, I. Takeuchi, A. M. Rappe, L. W. Martin, H. Wen, and A. M. Lindenberg, *Adv. Mater.* **27**, 6371 (2015).
- [26] S. Liu, I. Grinberg, and A. M. Rappe, *Nature* **534**, 360 (2016).
- [27] S. Liu, I. Grinberg, and A. M. Rappe, *Appl. Phys. Lett.* **103**, 232907 (2013).
- [28] R. Xu, S. Liu, I. Grinberg, J. Karthik, A. R. Damodaran, A. M. Rappe, and L. W. Martin, *Nature Mater.* **14**, 79 (2015).
- [29] G. Kwei, A. Lawson, S. Billinge, and S. Cheong, *J. Phys. Chem.* **97**, 2368 (1993).
- [30] O. Diéguez, S. Tinte, A. Antons, C. Bungaro, J. B. Neaton, K. M. Rabe, and D. Vanderbilt, *Phys. Rev. B* **69**, 212101 (2004).
- [31] A. Von Hippel, *Rev. Mod. Phys.* **22**, 221 (1950).
- [32] I. D. Brown, *Chem. Rev.* **109**, 6858 (2009).
- [33] I. Brown and R. Shannon, *Acta Crystallogr. A* **29**, 266 (1973).
- [34] I. Brown and K. K. Wu, *Acta Crystallogr. B* **32**, 1957 (1976).
- [35] M. Finnis and J. Sinclair, *Philos. Mag. A* **50**, 45 (1984).
- [36] M. A. Harvey, S. Baggio, and R. Baggio, *Acta Crystallogr. B* **62**, 1038 (2006).
- [37] P. Giannozzi, S. Baroni, N. Bonini, M. Calandra *et al.*, *J. Phys.: Condens. Matter* **21**, 395502 (2009).
- [38] J. P. Perdew, A. Ruzsinszky, G. I. Csonka, O. A. Vydrov, G. E. Scuseria, L. A. Constantin, X. Zhou, and K. Burke, *Phys. Rev. Lett.* **100**, 136406 (2008).
- [39] <http://opium.sourceforge.net>
- [40] H. J. Monkhorst and J. D. Pack, *Phys. Rev. B* **13**, 5188 (1976).
- [41] M. Parrinello and A. Rahman, *Phys. Rev. Lett.* **45**, 1196 (1980).
- [42] P. Ghosez, X. Gonze, P. Lambin, and J.-P. Michenaud, *Phys. Rev. B* **51**, 6765 (1995).
- [43] G. Geneste, *J. Phys.: Condens. Matter* **23**, 125901 (2011).
- [44] J. M. Vielma and G. Schneider, *J. Appl. Phys.* **114**, 174108 (2013).
- [45] R. E. Cohen and H. Krakauer, *Phys. Rev. B* **42**, 6416 (1990).
- [46] M. Gaudon, *Polyhedron* **88**, 6 (2015).
- [47] K. H. Ehses, H. Bock, and K. Fischer, *Ferroelectrics* **37**, 507 (1981).
- [48] C. Jun, F. Chan-Gao, L. Qi, and F. Duan, *J. Phys. C: Solid State Phys.* **21**, 2255 (1988).
- [49] R. Comes, M. Lambert, and A. Guinier, *Solid State Commun.* **6**, 715 (1968).
- [50] K. Itoh, L. Zeng, E. Nakamura, and N. Mishima, *Ferroelectrics* **63**, 29 (1985).
- [51] E. A. Stern, *Phys. Rev. Lett.* **93**, 037601 (2004).
- [52] K. J. Gaffney and H. N. Chapman, *Science* **316**, 1444 (2007).
- [53] N. A. Pertsev, A. G. Zembilgotov, and A. K. Tagantsev, *Phys. Rev. Lett.* **80**, 1988 (1998).
- [54] V. G. Koukhar, N. A. Pertsev, and R. Waser, *Phys. Rev. B* **64**, 214103 (2001).